Inverse scattering for frequency-scanned full-field optical coherence tomography

Daniel L. Marks, Tyler S. Ralston, Stephen A. Boppart, and P. Scott Carney

Beckman Institute of Advanced Science and Technology, 405 North Mathews, Urbana, Illinois 61801, USA

Received February 27, 2006; revised October 4, 2006; accepted October 25, 2006;
posted October 27, 2006 (Doc. ID 68379); published March 14, 2007

Full-field optical coherence tomography (OCT) is able to image an entire *en face* plane of scatterers simultaneously, but typically the focus is scanned through the volume to acquire three-dimensional structure. By solving the inverse scattering problem for full-field OCT, we show it is possible to computationally reconstruct a three-dimensional volume while the focus is fixed at one plane inside the sample. While a low-numerical-aperture (NA) OCT system can tolerate defocus because the depth of field is large, for high NA it is critical to correct for defocus. By deriving a solution to the inverse scattering problem for full-field OCT, we propose and simulate an algorithm that recovers object structure both inside and outside the depth of field, so that even for high NA the focus can be fixed at a particular plane within the sample without compromising resolution away from the focal plane. © 2007 Optical Society of America

OCIS codes: 100.3010, 110.4500.

1. INTRODUCTION

The capabilities of optical coherence tomography[1,2] (OCT) and optical coherence microscopy[3–5] (OCM) have been greatly extended by computed imaging and synthetic aperture techniques.[6] Among the recently demonstrated advantages is the ability to resolve features in the sample that are outside the confocal region. Ultimately, a more quantitatively accurate and faithful representation of the sample structure is provided. In this work, the inverse scattering problem in full-field OCT–OCM[7–15] is investigated. A variant where the focus remains fixed at the surface of the sample and computed imaging techniques are used to infer the structure is proposed. This modality obviates the requirement that the focus be scanned through the sample. A forward model is derived that relates the measured data to the object structure. From this model, a solution of the inverse scattering problem is obtained, thus providing a means to infer the object structure from the data. The achievable resolution and system bandpass are also derived. Finally, a simulation is presented that demonstrates the application of the method.

Full-field OCT is capable of imaging an entire plane of scatterers simultaneously, providing a very rapid way to acquire the sample structure. A typical full-field OCT system is built around a Michelson interferometer with a broadband illumination source (see Fig. 1). Reference and sample beams are derived from the source using a beam splitter. An extended area of the sample is illuminated by a broadband collimated beam through a microscope objective. The objective is focused at the depth of features of interest. A signal is scattered by the sample back through the objective. A reference beam is delayed to return to the beam splitter at the same time that the signal scattered from the sample in the focal plane arrives. The reference and signal are superimposed and focused on a focal-plane array (such as a CCD sensor) where the amplitude of the interference signal is measured. Only those scatterers within a coherence length of the focal plane produce scattered fields that will interfere with the reference. By recording the interference, an image of a slice of the sample around the focal plane is obtained, and the out-of-focus contributions are removed by coherence gating. The usual technique is then to translate the sample through the focal plane so that the scatterers at many different depths may be imaged and a 3-D structure obtained.

While this method can be used to obtain high-resolution images for the entire volumes of a sample quickly, it has a number of disadvantages. First, the sample and microscope objective must be translated relative to each other. This is relatively slow and requires fine positioning. Second, this method uses time-domain detection that produces a lower signal-to-noise ratio than Fourier-domain or frequency-swept OCT.[16–20]

When the reference arm is adjusted such that the reference field is synchronized with the scattered field returned from a plane other than (and far removed from) the focal plane, the interference image obtained at the CCD appears to be an image of the scatterers in that plane but out of focus. For a conventionally formed image, this would likely irreversibly impair the resulting image quality. However, wide-field OCT is an interferometric technique, and so the phase as well as the amplitude is measured. To bring an image into focus, it is simply necessary to appropriately rephase the field. To accomplish this, we will solve the linear inverse scattering problem. This serves the additional purpose of providing a quantitatively meaningful reconstruction of the entire object.

Instead of scanning the focus through the sample, we propose to fix the focus at the surface of the sample so that no relative translation is needed between the objective and the sample. A frequency-swept source can provide a new degree of freedom, replacing a degree of freedom lost by fixing the focus. Because the objective and sample may be left fixed relative to each other, no trans-

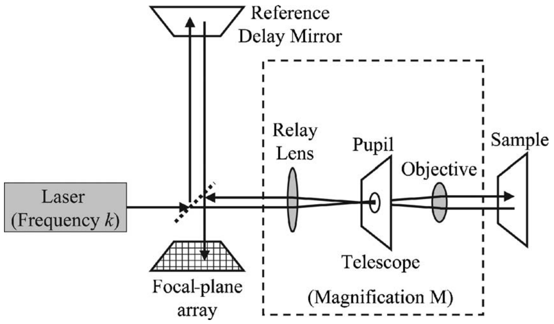

Fig. 1. Schematic diagram of full-field OCT using frequency scanning and the focus of the objective fixed at the sample surface.

lation hardware is needed, which makes placing the objective on a fiber optic or a handheld probe easier. While frequency-swept full-field OCT[21] has been achieved, typically the numerical aperture (NA) and hence the resolution is low so that the depth of field is very large and diffraction effects can be neglected. However, when a high NA is used, the depth of field is very short, and accounting for the defocus is necessary to preserve the resolution over the entire volume of interest.

To understand how computational image formation works in full-field OCT, in Section 2 a physical model for the scattering process is developed, and from this a relationship between the data and the object structure is derived. Based on this relationship, in Section 3, the inverse scattering problem is solved in order to infer the sample structure from the data. In Section 4, an analysis of the bandpass and resolving power of the system is given. In Section 5, the results are illustrated by a numerical simulation.

2. DERIVATION OF THE SCATTERING OPERATOR FOR FULL-FIELD OPTICAL COHERENCE TOMOGRAPHY

An illustration of the full-field OCT system being studied is shown in Fig. 1. This system is based on a Michelson interferometer, but other configurations such as a self-referencing Fizeau design could be used. In this system, the source is a tunable, narrowband laser. The laser is tuned to wavelengths λ that correspond to wavenumbers $k=2\pi/\lambda$. The laser ideally emits a plane wave (or is spatially filtered to produce one).

The laser illumination is split into two. One component travels to a reference mirror and is reflected back through the beam splitter to the output port where the focal-plane array is located. The other component is demagnified by a factor $1/M$, using a telescope of magnification M. The purpose of the telescope is to concentrate the illumination onto the sample and then relay a magnified scattered field to the focal-plane array. This telescope consists of two converging lenses, a relay lens and a microscope objective. The illumination on the sample is a normally incident plane wave. The sample scatters some radiation backward through the telescope. The telescope is aligned to afocally and telecentrically image[22] the front surface of the sample to the focal-plane array. The telescope is in effect two Fourier-transform lenses with possibly nonunity magnification.[23] Note that, unlike standard full-field OCT microscopy, the focus of the objective remains fixed at the surface of the sample. It is assumed that the telescope is aberration free and vignetting inside the telescope is negligible. If the telescope is assumed to correct spherical aberration, then there is a finite volume within the sample space for which these assumptions hold. A pupil is placed at the focus of the illumination beam inside the telescope to spatially filter the backscattered signal to enforce a well-defined spatial band limit. At the focal-plane array, the reference and sample signals superimpose and interfere, and the intensity of the interference is detected.

To derive the relationship between the object structure and the data detected on the sensor, a mathematical model of scattering of the illumination field by the object and interferometric detection at the sensor is developed below. A scalar field is substituted for the electromagnetic field, neglecting polarization effects. The incident field on the sample is given by the expression

$$E_i(\mathbf{r};k) = A(k)\exp(ik\mathbf{r}\cdot\hat{\mathbf{z}}), \tag{1}$$

where $\mathbf{r}$ is a location in the sample volume, k is the illumination wavenumber, $A(k)$ is the power spectral density of the illumination at frequency k, and $\hat{\mathbf{z}}$ is the direction of increasing depth into the sample. In this work, it is assumed that the scattering is well modeled by the first Born approximation. The susceptibility of the object is given by $\eta(\mathbf{r})$ such that $\eta(\mathbf{r})=0$ for $z<0$. The secondary scattered field $E_s(\mathbf{r}';k)$ from the object at the plane $z=0$ is given by the expression

$$E_s(\mathbf{r}';k) = \int_V \mathrm{d}^3r E_i(\mathbf{r};k)\,\eta(\mathbf{r})\frac{\exp(ik|\mathbf{r}'-\mathbf{r}|)}{|\mathbf{r}'-\mathbf{r}|}. \tag{2}$$

It is useful to define the 2-D Fourier transform $\tilde{E}_s(\mathbf{q};k) = \int \mathrm{d}^2r'\, E_s(\mathbf{r}';k)\exp(i\mathbf{q}\cdot\mathbf{r}')$ with $\mathbf{q}$ being a transverse spatial frequency such that $\mathbf{q}\cdot\hat{\mathbf{z}}=0$. Using the plane-wave expansion of a spherical wave, Eq. (2) is recast to read

$$\tilde{E}_s(\mathbf{q};k) = 2\pi i A(k)\int_V \mathrm{d}^3r\,\eta(\mathbf{r})\exp\{i[\mathbf{q}\cdot\mathbf{r}] + iz[k+k_z(\mathbf{q})]\}k_z(\mathbf{q})^{-1}, \tag{3}$$

where $k_z(\mathbf{q})=\sqrt{k^2-q^2}$. The 3-D Fourier transform is defined such that $\tilde{\eta}(\mathbf{Q}) = \int_V \mathrm{d}^3r\ \eta(\mathbf{r})\exp(i\mathbf{Q}\cdot\mathbf{r})$. It is then found that the right-hand integral can be expressed in terms of $\tilde{\eta}(\mathbf{Q})$:

$$\tilde{E}_s(\mathbf{q};k) = 2\pi i A(k)k_z(\mathbf{q})^{-1}\tilde{\eta}\{\mathbf{q}+\hat{\mathbf{z}}[k+k_z(\mathbf{q})]\}. \tag{4}$$

The field $E_f(\mathbf{r};k)$ is produced by the propagation of $E_s(\mathbf{r}';k)$ through the telescope to the focal-plane array. Because the telescope is assumed to be an aberration-free telescope that afocally and telecentrically images the plane at the sample $z=0$ to the focal-plane array in the plane $z=z_f$, its function can be modeled as a simple convolution with a point-spread function accounting for the finite bandwidth of the telescope and a magnification factor given by M. The field at the focal-plane array is given by $E_f(\mathbf{r};k)$, and the point-spread function of the telescope is given by $P(\mathbf{r};k)$. The relationship between $E_f(\mathbf{r};k)$ and $E_s(\mathbf{r}';k)$ is thus

$$E_f(\mathbf{r};k) = M^{-1}\int \mathrm{d}^2r' E_s(\mathbf{r}';k)P(\mathbf{r}/M-\mathbf{r}';k). \tag{5}$$

We further define the Fourier transforms $\tilde{E}_f(\mathbf{q};k) = \int_{z=z_f}\mathrm{d}^2r\, E_f(\mathbf{r};k)\exp(i\mathbf{q}\cdot\mathbf{r})$ and the coherent transfer function of the telescope $\tilde{P}(\mathbf{q};k)=\int\mathrm{d}^2r\, P(\mathbf{r};k)\exp(i\mathbf{q}\cdot\mathbf{r})$. Thus the convolution in Eq. (5) is expressed as

$$\begin{aligned}\tilde{E}_f(\mathbf{q};k) &= M\tilde{E}_s(M\mathbf{q};k)\tilde{P}(M\mathbf{q};k)\\ &= 2\pi i M A(k)\tilde{P}(M\mathbf{q};k)k_z(M\mathbf{q})^{-1}\\ &\quad\times\tilde{\eta}\{M\mathbf{q}+\hat{\mathbf{z}}[k+k_z(M\mathbf{q})]\}.\end{aligned} \tag{6}$$

Equation (6) specifies a relationship between Fourier components of the field on the focal-plane array and those of the object susceptibility.

The reference mirror is placed to effect a delay of τ relative to the total delay required for the beam to travel from the beam splitter to the plane $z=0$ in the sample arm and back. The reference field $E_r(\mathbf{r};k,\tau)$ relayed to the focal-plane array is then given by

$$E_r(\mathbf{r};k,\tau) = A(k)\exp[i\omega(k)\tau], \tag{7}$$

where $\omega(k)$ is a dispersion relation relating the temporal frequency to the spatial frequency in the sample medium. For example, if the sample medium is vacuum, then $\omega(k)=kc$, where c is the speed of light in vacuum. The intensity $I(\mathbf{r};\mathbf{k},\tau)=|E_r(\mathbf{r};k,\tau)+E_f(\mathbf{r};k)|^2$ on the focal-plane array is then given by the expression

$$\begin{aligned}I(\mathbf{r};k,\tau) &= |A(k)|^2 + |E_f(\mathbf{r};k)|^2 + 2A(k)\mathrm{Re}\{E_f(\mathbf{r};k)\\ &\quad\times\exp[-i\omega(k)\tau]\}.\end{aligned} \tag{8}$$

The part of the signal that is due to interference between the signal and the reference beams is defined as the data function $D(\mathbf{r};k)=A(k)E_f(\mathbf{r};k)$. The complex quantity $D(\mathbf{r};k)$ can be estimated from measurements of $I(\mathbf{r};k,\tau)$ at multiple values of the delay τ. For example, three measurements of $I(\mathbf{r};k,\tau)$ such that $\omega\tau=0$, $\pi/2$, and π may be summed to yield

$$D(\mathbf{r};k) = \frac{1-i}{4}I(\mathbf{r};k,0) - \frac{1+i}{4}I(\mathbf{r};k,\pi/\omega) + \frac{i}{2}I(\mathbf{r};k,\pi/2\omega). \tag{9}$$

This method of phase-shifting interferometry is well known.[24] Inserting the results of Eq. (6), we can express the Fourier transform of the data function, which is $\tilde{D}(\mathbf{q};k)=\int\mathrm{d}^2r\, D(\mathbf{r};k)\exp(i\mathbf{q}\cdot\mathbf{r})$, as

$$\tilde{D}(\mathbf{q};k) = \tilde{K}(\mathbf{q};k)\tilde{\eta}\{M\mathbf{q}+\hat{\mathbf{z}}[k+k_z(M\mathbf{q})]\}, \tag{10}$$

where for convenience the bandpass function $\tilde{K}$ is defined

$$\tilde{K}(\mathbf{q},k) = 2\pi i M A(k)^2\tilde{P}(M\mathbf{q};k)k_z^{-1}(M\mathbf{q}). \tag{11}$$

Thus the data are expressed in terms of the 3-D Fourier transform of the sample structure, and so the resolution of the reconstruction of the sample structure is space invariant. However, vignetting and aberrations in the telescope limit the volume over which this resolution can be obtained. As long as the center of the volume of interest is along the axis of the objective and on the focal plane of the objective, and the extent of the volume is much smaller than the field size the objective is corrected for, the aberrations and vignetting of the telescope can be neglected, and the resolution can be considered space invariant. However, for a sufficiently large volume of interest the resolution of the instrument becomes space variant and sensitive to the specific vignetting and aberration properties of the objective used.

When obtaining an inverse scattering solution, it is desirable to express Eq. (10) in the operator notation used for formal statements of relationships between functions because formal inverse scattering solutions are commonly expressed in terms of such operators. We define an operator $\tilde{\mathbf{K}}$ such that $\tilde{\mathbf{D}}=\tilde{\mathbf{K}}\tilde{\boldsymbol{\eta}}$, which relates the sample susceptibility Fourier representation $\tilde{\boldsymbol{\eta}}$ to the data Fourier representation $\tilde{\mathbf{D}}$ with the relationship of Eq. (10). We define the axial component of $\beta=\mathbf{Q}\cdot\hat{\mathbf{z}}$ and the transverse component of $\mathbf{Q}$ as $\mathbf{Q}_\parallel=\mathbf{Q}-\hat{\mathbf{z}}\beta$. The operator $\tilde{\mathbf{K}}$ is then given by

$$\begin{aligned}\tilde{\mathbf{D}} &= \tilde{\mathbf{K}}\tilde{\boldsymbol{\eta}}\\ &= \int \mathrm{d}^3Q\,\tilde{K}(\mathbf{q};k)\tilde{\eta}(\mathbf{Q})\delta^{(2)}(\mathbf{Q}_\parallel - M\mathbf{q})\delta[\beta-k-k_z(M\mathbf{q})],\end{aligned} \tag{12}$$

where the delta functions enforce the conditions of the coordinate transformation. This operator concisely contains both the kernel and the coordinate transformations expressed in Eq. (10).

To obtain the measurements needed to reconstruct $\eta(\mathbf{r})$, one must vary both k and τ. In practice, however, it is often slow and inconvenient to adjust both. If one is willing to tolerate some image artifacts, just one of these parameters need be scanned. For simplicity, it is assumed that the pupil function $P(\mathbf{r}';k)$ is real and symmetric, which is often the case (for example, with a circular pupil), so that $\tilde{P}(\mathbf{q};k)$ is likewise real and symmetric.

One may decide to hold the reference delay position fixed such that $\tau=0$ to avoid translating the mirror. In this case phase shifting is not performed, and the imaginary component of $D(\mathbf{r};k)$ is not obtainable. If the imaginary part of $D(\mathbf{r};k)$ is assumed to be zero, then due to the Hermitian symmetry of the Fourier transform of real functions $\tilde{D}(-\mathbf{q},k)=\tilde{D}(\mathbf{q},k)^*$. The function $\tilde{\eta}(\mathbf{Q})$ then also has Hermitian symmetry reflected over the axis $|\mathbf{q}|=0$. The effect is that a conjugate image of the susceptibility is present, reflected across the plane $z=0$. Because the delay $\tau=0$ corresponds to the plane $z=0$, as long as the entire sample is contained in the half-space $z>0$, the conjugate image and the real image do not overlap. In addition, there is an artifact corresponding to the term $|E_f(\mathbf{r};k)|^2$ in Eq. (8). If the magnitude of the sample signal is small relative to the reference signal, the magnitude of this artifact is also small compared with the real image and can be neglected.

For completeness, we note that the method of inverse scattering can be applied to time-domain full-field OCT as well. If the delay τ is scanned as occurs in time-domain full-field OCT and the laser emits all wavenumbers k simultaneously (such as occurs in a mode-locked laser or a spontaneous emission source typical of time-domain OCT), the signal $I_T(\mathbf{r};\tau)$ is the sum of the interference patterns over all emitted frequencies:

$$I_T(\mathbf{r};\tau)=\frac{1}{2\pi}\left[\int_{-\infty}^{\infty}\mathrm{d}k\left(\frac{\mathrm{d}\omega}{\mathrm{d}k}\right)(|A(k)|^2+|E_f(\mathbf{r};k)|^2)\right]+\frac{1}{\pi}\mathrm{Re}\left\{\int_{-\infty}^{\infty}\mathrm{d}k\left(\frac{\mathrm{d}\omega}{\mathrm{d}k}\right)D(\mathbf{r};k)\exp[-i\omega(k)\tau]\right\}. \tag{13}$$

The term in square brackets is a background intensity that is independent of τ and therefore is easily subtracted to remove its contribution from the measured intensity. Neglecting the background intensity and the slowly varying Jacobian $(\mathrm{d}\omega/\mathrm{d}k)$, Eq. (13) relates the real part of the inverse Fourier transform of $D(\mathbf{r};k)$ with respect to k to the total intensity $I_T(\mathbf{r};\tau)$. To be able to remove the Re{ } operation so that a unique solution for $D(\mathbf{r};k)$ can be found, one equates $D(\mathbf{r};-k)=D(\mathbf{r};k)^*$. Equation (10) then likewise enforces Hermitian symmetry on $\tilde{\eta}(-\mathbf{Q})=\tilde{\eta}(\mathbf{Q})^*$. Therefore in this case the reconstructed susceptibility is assumed to be real valued.

In this derivation, the focal plane of the objective and the front surface of the sample are assumed to coincide. This assumption has simplified the preceding analysis and presentation, but it is not required. If the sample is placed such that the focus is below the sample surface by a distance z_0, but the delay produced by the reference coincides with the delay of the sample surface, the data can be modified to account for the displacement. In particular, the modified data $\tilde{D}'(\mathbf{q};k)$ are related to the sampled data $\tilde{D}(\mathbf{q};k)$ by

$$\tilde{D}'(\mathbf{q};k)=\tilde{D}(\mathbf{q};k)\exp\{iz_0[k-k_z(M\mathbf{q})]\}. \tag{14}$$

This formula can be found by noting that the field relayed by the telescope is now situated at the plane $z=z_0$, introducing a factor $\exp\{-iz_0[k+k_z(M\mathbf{q})]\}$ to the right-hand side of Eq. (3). At the same time, the delay reference mirror must be moved a distance z_0 further from the beam splitter so that the new effective delay corresponds to the front surface of the sample, including a factor of $\exp(-2ikz_0)$ to the right-hand side of Eq. (7) to place the reference delay coincident with the front surface of the sample. Effectively, the measured field is computationally propagated at each frequency to the surface of the sample.

3. INVERSE SCATTERING IN FULL-FIELD OPTICAL COHERENCE TOMOGRAPHY

Using the developed mathematical model, a solution to the inverse scattering problem may be derived. In general, the problem is ill posed, and so regularization techniques will need to be used to produce a stable solution. Because the forward problem is linear, we derive a linearized inverse based on least-squares error. To do so, we first specify the complete forward operator $\mathbf{K}$ such that $\mathbf{D}=\mathbf{K}\boldsymbol{\eta}$, which relates the data to the object structure

$$D(\mathbf{r};k)=\mathbf{K}\boldsymbol{\eta}=\int\mathrm{d}^3r'K(\mathbf{r}',\mathbf{r};k)\,\eta(\mathbf{r}'), \tag{15}$$

where the kernel $K(\mathbf{r}';\mathbf{r};k)$ of the operator $\mathbf{K}$ is given by

$$K(\mathbf{r}',\mathbf{r};k)=M^{-1}A(k)^2\exp(ik\mathbf{r}'\cdot\hat{\mathbf{z}})\times\int_{\mathbf{r}''\cdot\hat{\mathbf{z}}=0}\mathrm{d}^2r''\frac{\exp(ik|\mathbf{r}''-\mathbf{r}'|)}{|\mathbf{r}''-\mathbf{r}'|}P(\mathbf{r}/M-\mathbf{r}'';k). \tag{16}$$

Given this relationship between the data and the object, the pseudoinverse solution $\eta^+(\mathbf{r})$ for object susceptibility is

$$\eta^+(\mathbf{r})=\arg\min_{\eta}|\mathbf{D}-\mathbf{K}\boldsymbol{\eta}|^2=\arg\min_{\eta}\int\mathrm{d}^2r'\int\mathrm{d}k|D(\mathbf{r}';k)-\mathbf{K}\eta(\mathbf{r})|^2. \tag{17}$$

Expressed in operator notation, the solution to this least-squares problem is given by the pseudoinverse $\boldsymbol{\eta}^+=(\mathbf{K}^*\mathbf{K})^{-1}\mathbf{K}^*\mathbf{D}$, where $\mathbf{K}^*$ is the Hermitian conjugate of $\mathbf{K}$ and $\mathbf{K}^*\mathbf{K}$ is assumed to be invertible. It is much simpler to formulate the least-squares problem in the Fourier domain, using the operator $\tilde{\mathbf{K}}$ of Eq. (12). In terms of the operator $\tilde{\mathbf{K}}$, the Tikhonov-regularized least-squares solution $\tilde{\boldsymbol{\eta}}^+=(\tilde{\mathbf{K}}^*\tilde{\mathbf{K}}+\gamma\mathbf{I})^{-1}\tilde{\mathbf{K}}^*\tilde{\mathbf{D}}$, with the positive constant γ being the regularization parameter. The adjoint is explicitly given by the expression

$$\begin{aligned}\tilde{\boldsymbol{\eta}}_A=\tilde{\mathbf{K}}^*\tilde{\mathbf{D}}&=\int\mathrm{d}^2q\int\mathrm{d}k\tilde{K}^*(\mathbf{q};k)\tilde{D}(\mathbf{q};k)\,\delta^{(2)}\\&\quad\times(\mathbf{Q}_\parallel-M\mathbf{q})\,\delta[\beta-k-k_z(M\mathbf{q})]\\&=\tilde{K}^*\left(M^{-1}\mathbf{Q}_\parallel;\frac{Q_\parallel^2+\beta^2}{2\beta}\right)\\&\quad\times\tilde{D}\left(M^{-1}\mathbf{Q}_\parallel;\frac{Q_\parallel^2+\beta^2}{2\beta}\right)M^{-2}\frac{\beta}{\beta+\sqrt{\beta^2+Q_\parallel^2}},\end{aligned} \tag{18}$$

with $\tilde{K}(\mathbf{q};k)$ taken from Eq. (11). Given the expressions for $\tilde{\mathbf{K}}$ and $\tilde{\mathbf{K}}^*$, the solution $\tilde{\boldsymbol{\eta}}^+$ is given by

$$\tilde{\eta}^+(\mathbf{Q})=\frac{\tilde{D}\left(M^{-1}\mathbf{Q}_\parallel;\frac{Q_\parallel^2+\beta^2}{2\beta}\right)\tilde{K}^*\left(M^{-1}\mathbf{Q}_\parallel;\frac{Q_\parallel^2+\beta^2}{2\beta}\right)}{\left|\tilde{K}\left(M^{-1}\mathbf{Q}_\parallel;\frac{Q_\parallel^2+\beta^2}{2\beta}\right)\right|^2+\gamma M^2\frac{\beta_+\sqrt{\beta^2+Q_\parallel^2}}{\beta}}. \tag{19}$$

4. RESOLUTION AND BANDPASS

Equation (10) expresses a relationship between the 2-D Fourier transform of the data and the 3-D Fourier transform of the object. As mentioned previously, this relationship implies that the resolution of the reconstructed object is space invariant. With suitable specifications of the instrument, one can identify the region of the Fourier space of the structure function that can be sampled. This region is called the band volume and is an analogue to the band limit of 1-D signals, except that the band volume consists of the interior of a shape in 3-D Fourier space rather than just a 1-D interval.

There are two specifications of the instrument that determine the shape of the band volume. The first is the bandwidth of the illumination, which is specified by the interval of frequencies $k_{min} < k < k_{max}$. The other parameter is the numerical aperture (NA) of the imaging system $0 < \mathrm{NA} < 1$. A particular NA implies a pupil bandpass:

$$\tilde{P}(\mathbf{q};k) = 1 \qquad \text{for } |\mathbf{q}| \leq (\mathrm{NA})k,$$

$$\tilde{P}(\mathbf{q};k) = 0 \qquad \text{for } |\mathbf{q}| > (\mathrm{NA})k. \tag{20}$$

These inequalities constrain the volume of the data function $\tilde{D}(\mathbf{q};k)$ that can be sampled. The band volume is the intersection of the volumes defined by the two inequalities expressed in terms of the object 3-D spatial frequency $\mathbf{Q}$:

$$k_{min} < Q^2/(2\mathbf{Q}\cdot\hat{\mathbf{z}}) < k_{max},$$

$$(2\mathbf{Q}\cdot\hat{\mathbf{z}})\sqrt{Q^2 - (\mathbf{Q}\cdot\hat{\mathbf{z}})^2}/Q^2 < \mathrm{NA}. \tag{21}$$

Figure 2 shows an example of a band volume for an instrument with 0.5 NA and bandwidth from $0.8k_{max} < k < k_{max}$. There are two views so that both the top and the bottom surfaces are visible. The top and bottom surfaces are spherical (with different radii and centers), and the side surface is a right circular cone with its vertex at the origin.

In the limit of small bandwidth and low NA, the band volume shape approaches that of a circular cylinder. In this limit, the resolution in the axial direction is determined solely by the bandwidth, and the transverse resolution is determined by the NA, as is normally assumed in OCT. However, the band volume becomes less cylindrical and more cone shaped as the NA and bandwidth increase, and axial and transverse resolutions are dependent on both the bandwidth and the NA.

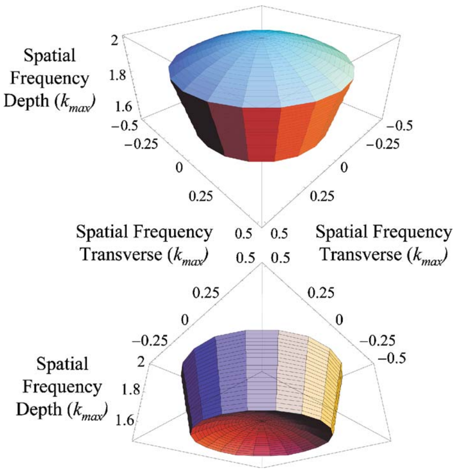

Fig. 2. (Color online) Calculated band volume shape for a full-field OCT system. All units are in terms of the maximum spatial frequency of the illumination.

5. SIMULATION

To demonstrate the expected performance of inverse scattering in full-field OCT, a simulation was performed. An object consisting of randomly placed point scatterers was imaged with a simulated full-field OCT system, and then the structure of the object was reconstructed from the data. The simulated object volume cross-sectional area was 25 wavelengths in depth and 40 by 40 wavelengths in the transverse direction. The illumination source had a Gaussian spectrum with a 40% fractional full width at half-maximum bandwidth (corresponding, for example, to 320 nm of bandwidth centered at 800 nm, which can be achieved by a Ti-sapphire laser).[25–27] The simulated NA of the imaging objective was 0.5.

Data were synthesized by first calculating the scattered field $E_s(\mathbf{r}';k)$ using Eq. (2), where the object $\eta(\mathbf{r})$ was taken to be a collection of randomly chosen discrete points. The synthetic interferograms were calculated as a function of illumination spatial frequency that corresponds to how the data would be acquired from a swept source. Then the synthesized data function was calculated using the relation $\tilde{D}(\mathbf{q};k) = A(k)\tilde{E}_s(\mathbf{q};k)\tilde{P}(\mathbf{q};k)$, where $\tilde{E}_s(\mathbf{q};k)$ was obtained from $E_s(\mathbf{r}';k)$ by a 2-D Fourier transform. Finally, a 2-D inverse Fourier transform yielded $D(\mathbf{r}';k)$. By assembling the synthetic data by superimposing the signals produced by discrete scatterers, the accuracy of the resampling-based inverse method could be better verified because the synthetic data were computed without resampling.

The synthetic data are shown in Fig. 3. Figure 3(a) shows $D(\mathbf{r};k)$, which describes the data that would be recorded on the focal-plane array. Because this is difficult to interpret, we have also included in Fig. 3(b) the time-domain signal $I_T(\mathbf{r};\tau)$ given by Eq. (13), which appears to more directly represent the underlying object. It may be seen in the plots of $I_T(\mathbf{r};\tau)$ that as the delay τ is increased the planes more distant from the focus are acquired and manifest increasing distortion. This corresponds to the standard degradation one expects from defocus when inverse scattering is not used.

The following steps were followed to compute the image estimate $\eta^{+}(\mathbf{r})$ from the synthetic data $D(\mathbf{r};k)$:

1. $\tilde{D}(\mathbf{q};k)$ was computed from $D(\mathbf{r};k)$ using the 2-D Fourier transform.
2. The kernel $\tilde{K}(\mathbf{q};k)$ was calculated using Eq. (11).
3. Equation (19) was used to compute $\tilde{\eta}^{+}(\mathbf{q};k)$ from $\tilde{K}(\mathbf{q};k)$ and $\tilde{D}(\mathbf{q};k)$.
4. The function $\tilde{\eta}^{+}(\mathbf{q};k)$, which is uniformly sampled in the variables $\mathbf{q}$ and k, is resample to be uniformly sampled in the variables $\mathbf{q}$ and β using the relation $k = (M^2q^2 + \beta^2)/2\beta$. The resampled version is $\tilde{\eta}^{+}(\mathbf{Q})$, where the transverse component of $\mathbf{Q}$ is $M\mathbf{q}$ and the axial component is β.
5. The 3-D inverse Fourier transform of $\tilde{\eta}^{+}(\mathbf{Q})$ is performed to find $\eta(\mathbf{r})$.

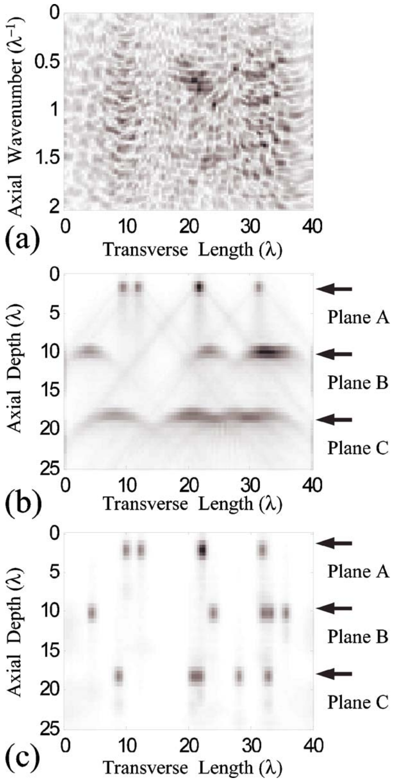

Fig. 3. (Color online) Simulation of inverse scattering in full-field OCT. (a) The magnitude of the raw interference patterns recorded as a function of illumination spatial frequency. (b) A projection of the time-domain data for a collection of randomly placed point scatterers imaged with full-field OCT. (c) A projection of the computed reconstruction of the scatterers. All length units are in the center wavelength of the illumination, and spatial frequencies are inverse wavelength units. Three planes are denoted that are shown as *en face* images in Fig. 5.

The resampling step (step 4) is the key step in compensating for out-of-focus diffraction effects and therefore needs further discussion. Equation (10) specifies a relationship between $\tilde{D}(\mathbf{q};k)$ and $\tilde{\eta}(\mathbf{Q})$. In the continuously sampled case, there is a one-to-one correspondence between values of $\tilde{D}$ and $\tilde{\eta}$ so that this relation is straightforward. However, in practice the data $D(\mathbf{r};k)$ is discretely sampled and is typically uniform in $\mathbf{r}$ and k. The Fourier data $\tilde{D}(\mathbf{q};k)$ are therefore sampled uniformly in $\mathbf{q}$ and k. However, the reconstructed Fourier data of the susceptibility $\tilde{\eta}^{+}(\mathbf{Q})$ need to be uniform in $\mathbf{q}$ and β so that the 3-D inverse Fourier transform can recover a uniformly sampled reconstruction of $\eta(\mathbf{r})$. The resampling step interpolates points on the function $\tilde{\eta}^{+}(\mathbf{q};k)$ that are uniformly spaced in β. Figure 4 is a plot of the points on a given function that are sampled in the forward and inverse problems. Each of the intersections of grid curves indicates a point on the function that is interpolated to form the resampled function. Figure 4(a) is the resampling that maps from 3-D object space $\mathbf{Q}_{\parallel},\beta$ to the data space $\mathbf{q},k$ for the forward problem. Figure 4(b) is the resampling from the data space $\mathbf{q},k$ to the object space $\mathbf{Q}_{\parallel},\beta$. The resampling occurs only along lines of constant $\mathbf{q}$, so that only 1-D interpolation is needed. In this simulation, a 1-D cubic B-spline interpolator was used to interpolate from the coordinates $\mathbf{q}+\hat{\mathbf{z}}[k+k_z(\mathbf{q})]$ to $\mathbf{Q}$ as shown in Eq. (19).

Finally, after the 3-D inverse Fourier transform of $\tilde{\eta}^{+}(\mathbf{Q})$ is taken, the reconstruction $\eta^{+}(\mathbf{r})$ results, which is shown in Fig. 3(c). As can be seen, the reconstruction corrects for diffraction and produces pointlike images. Figure 5 shows three *en face* planes corresponding to the depths A, B, and C marked in Fig. 3. The left column is the time-domain data measured in each of the *en face* planes, and the right column is the image of the scatterers computed by inverse scattering. Planes that are further from the focus appear to exhibit poorer resolution when viewed in the raw data because of the effect of defocus. One can also see the interference fringes between the images of adjacent scatterers. Despite the interference between scatterers, each point is clearly resolved with space-invariant

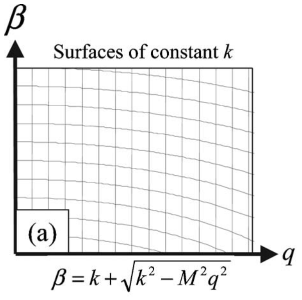

Fig. 4. (a) Resampling grid to compute synthetic data $\tilde{D}(\mathbf{q};k)$ from object $\tilde{\eta}(\mathbf{Q})$. (b) Resampling grid to compute reconstruction of $\tilde{\eta}(\mathbf{Q})$ from $\tilde{D}(\mathbf{q};k)$. Note that the transverse components of $\mathbf{Q}$ are the same as $M\mathbf{q}$, and the axial component of $\mathbf{Q}$ is β. To form the full 3-D Fourier space, both grids are revolved around their respective vertical axes.

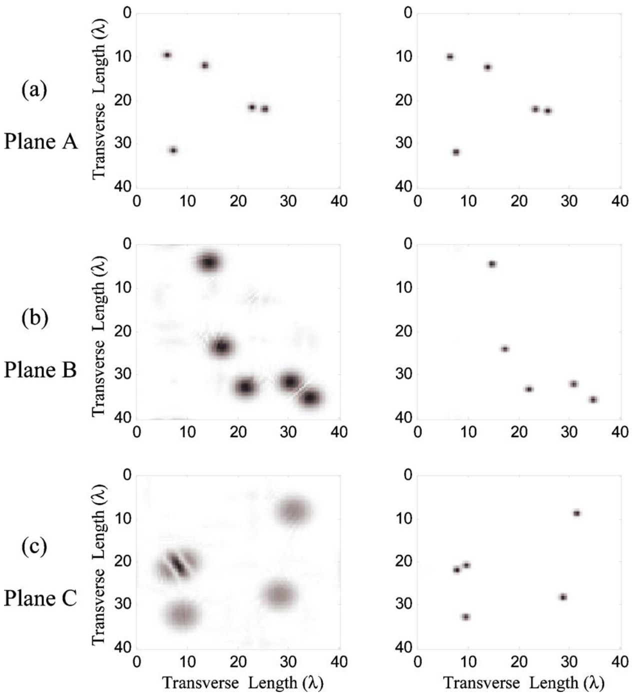

Fig. 5. (Color online) Three pairs of *en face* images of the time-domain data (left) and the reconstructed volume (right). (a)–(c) Pairs of images corresponding, respectively, to the planes A, B, and C marked in Fig. 3. All dimensions are in wavelength units.

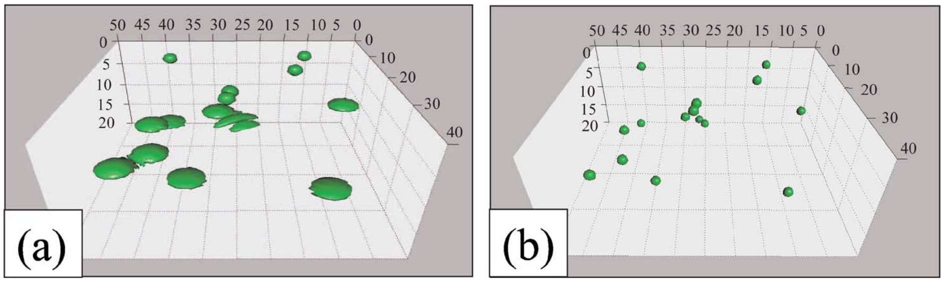

Fig. 6. (Color online) Three-dimensional volumes representing the (a) time-domain data and (b) reconstructed volume. All dimensions are in wavelength units.

resolution in the reconstructed image. This shows the algorithm correctly separates the interference patterns from scatterers to produce high-resolution images.

To show the overall improvement to the data, Fig. 6 is volume isosurface plots of the raw data in Fig. 6(a) and the reconstructed computed image in Fig. 6(b). Again, the blurring of the data is increasingly apparent with increasing distance from the focus plane at the top of the volume. In addition, stripelike features can be seen for the isosurfaces corresponding to interfering scatterers. This method can correct for the diffraction effects and produce pointlike images in Fig. 6(b) for each of the scatterers. The planes of the scatterers need not be so widely separated for the algorithm to distinguish them, but this was deliberately done to make the diffraction effects easier to visualize.

6. CONCLUSION

We have derived and demonstrated a method of performing inverse scattering in full-field OCT to reconstruct images of out-of-focus planes, which obviates the need to scan the focus through the volume. The solution of the inverse scattering problem implies that, neglecting vignetting and aberrations, the achievable resolution is space invariant and is the same away from the focus plane as at the focal plane. Vignetting limits the volume over which the resolution is space invariant because the solid angle over which the scattered light is collected decreases at points further from the objective aperture. Other factors limiting reconstruction quality are multiple scattering within the sample and sample motions during data acquisition causing phase error. This method may lead to faster and more accurate full-field OCT imaging because data acquisition can be very rapid, requiring only that the 2-D interferogram be sampled while the frequency of the source is scanned. As data acquisition speed and computational speed continue to increase, perhaps video-rate scanning of 3-D volumes will become possible.

Inverse scattering in full-field OCT also offers a signal-to-noise advantage over scanned beam OCT. In conventional scanned beam OCT, which utilizes a focused Gaussian beam rather than plane-wave illumination, it was shown[6] that the magnitude of the signal captured from scatterers away from the focus is inversely proportional to the distance from the focus. In practice, this places a limit on the axial range of the sample that can be imaged before the signal-to-noise ratio becomes unacceptable. There is no such attenuation of the signal away from the focus in the full-field OCT case. However, this advantage may be offset because full-field OCT may be less able to discriminate between single-scattering and multiply scattered photons because of its multimode detection.

ACKNOWLEDGMENTS

This research was supported in part by the National Science Foundation (BES 03-47747, S. A. Boppart) and the National Institutes of Health (National Institute of Biomedical Imaging and Bioengineering) (1 R01 EB00108, S. A. Boppart). P. S. Carney is supported in part by a National Science Foundation Faculty Early Career Development (CAREER) award (ECS 02-39265). Additional information can be found at http://biophotonics.uiuc.edu/.

S. A. Boppart can be reached by phone, 1-217-244-7479; fax, 1-217-244-1995; or e-mail, boppart@uiuc.edu. D. L. Marks can be reached by e-mail at dmarks@uiuc.edu.

REFERENCES

1. D. Huang, E. A. Swanson, C. P. Lin, J. S. Schuman, W. G. Stinson, W. Chang, M. R. Hee, T. Flotte, K. Gregory, C. A. Puliafito, and J. G. Fujimoto, "Optical coherence tomography," Science **254**, 1178–1181 (1991).
2. S. A. Boppart, B. E. Bouma, C. Pitris, J. F. Southern, M. E. Brezinski, and J. G. Fujimoto, "*In vivo* cellular optical coherence tomography imaging," Nat. Med. **4**, 861–864 (1998).
3. J. A. Izatt, M. R. Hee, G. M. Owen, E. A. Swanson, and J. G. Fujimoto, "Optical coherence microscopy in scattering media," Opt. Lett. **19**, 590–592 (1994).
4. J. M. Schmitt, M. J. Yadlowsky, and R. F. Bonner, "Subsurface imaging of living skin with optical coherence microscopy," Dermatology (Basel) **191**, 93–98 (1995).
5. J. A. Izatt, H.-W. Kulkarni, K. Wang, M. W. Kobayashi, and M. W. Sivak, "Optical coherence tomography and microscopy in gastrointestinal tissues," IEEE J. Sel. Top. Quantum Electron. **2**, 1017–1028 (1996).
6. T. S. Ralston, D. L. Marks, P. S. Carney, and S. A. Boppart, "Inverse scattering problem for optical coherence tomography," J. Opt. Soc. Am. A **23**, 1027–1037 (2006).
7. E. Beaurepaire and A.-C. Boccara, "Full-field optical coherence microscopy," Opt. Lett. **23**, 244–246 (1998).
8. A. Dubois, L. Vabre, A.-C. Boccara, and E. Beaurepaire, "High-resolution full-field optical coherence tomography with a Linnik microscope," Appl. Opt. **41**, 805–812 (2002).
9. A. Dubois, K. Grieve, G. Moneron, R. Lecaque, L. Vabre, and C. Boccara, "Ultrahigh-resolution full-field optical coherence tomography," Appl. Opt. **43**, 2874–2883 (2004).
10. A. Dubois, G. Moneron, K. Grieve, and A.-C. Boccara, "Three-dimensional cellular-level imaging using full-field optical coherence tomography," Phys. Med. Biol. **49**, 1227–1234 (2004).
11. K. Grieve, A. Dubois, M. Simonutti, M. Paques, J. Sahel,

J.-F. Le Gargasson, and C. Bocarra, "*In vivo* anterior segment imaging in the rat eye with high speed white light full-field optical coherence tomography," Opt. Express **13**, 6286–6295 (2005).

12. B. Laude, A. De Martino, B. Drevillon, L. Benattar, and L. Schwartz, "Full-field optical coherence tomography with thermal light," Appl. Opt. **41**, 6637–6645 (2002).
13. G. Moneron, A.-C. Bocarra, and A. Dubois, "Stroboscopic ultrahigh-resolution full-field optical coherence tomography," Opt. Lett. **30**, 1351–1353 (2005).
14. J. Moreau, V. Lorlette, and A.-C. Bocarra, "Full-field birefringence imaging by thermal-light polarization-sensitive optical coherence tomography. II. Instrument and results," Appl. Opt. **42**, 3811–3818 (2003).
15. Y. Watanabe, Y. Hayasaka, M. Sato, and N. Tanno, "Full-field optical coherence tomography by achromatic phase shifting with a rotating polarizer," Appl. Opt. **44**, 1387–1392 (2005).
16. R. Leitgeb, C. K. Hitzenberger, and A. F. Fercher, "Performance of Fourier domain vs. time domain optical coherence tomography," Opt. Express **11**, 889–894 (2003).
17. M. Choma, M. Sarunic, Y. Changhuei, and J. Izatt, "Sensitivity advantage of swept source and Fourier domain optical coherence tomography," Opt. Express **11**, 2183–2189 (2003).
18. P. Blazkiewicz, M. Gourlay, J. R. Tucker, A. D. Rakic, and A. V. Zvyagin, "Signal-to-noise ratio study of full-field Fourier-domain optical coherence tomography," Appl. Opt. **34**, 7722–7729 (2005).
19. A. V. Zvyagin, "Fourier-domain optical coherence tomography: optimization of signal-to-noise ratio in full space," Opt. Commun. **242**, 97–108 (2004).
20. A. V. Zvyagin, P. Blazkiewicz, and J. Vintrou, "Image reconstruction in full-field Fourier-domain optical coherence tomography," J. Opt. A **7**, 350–356 (2005).
21. B. Povazay, A. Unterhuber, B. Hermann, H. Sattmann, H. Arthaber, and W. Drexler, "Full-field time-encoded frequency-domain optical coherence tomography," Opt. Express **14**, 7661–7669 (2006).
22. D. N. Sitter, Jr. and W. T. Rhodes, "Three-dimensional imaging: a space invariant model for space variant systems," Appl. Opt. **29**, 3789–3794 (1990).
23. J. Goodman, *Introduction to Fourier Optics* (McGraw-Hill, 1968).
24. P. Hariharan, *Optical Interferometry* (Academic, 2003).
25. B. E. Bouma, G. J. Tearney, S. A. Boppart, M. R. Hee, M. E. Brezinski, and J. G. Fujimoto, "High-resolution optical coherence tomographic imaging using a mode-locked Ti:Al_2O_3 laser," Opt. Lett. **20**, 1486–1488 (1995).
26. W. Drexler, U. Morgner, F. X. Kartner, C. Pitris, S. A. Boppart, X. Li, E. P. Ippen, and J. G. Fujimoto, "*In vivo* ultrahigh-resolution optical coherence tomography," Opt. Lett. **24**, 1221–1223 (1999).
27. D. L. Marks, A. L. Oldenburg, J. J. Reynolds, and S. A. Boppart, "Study of an ultrahigh-numerical-aperture fiber continuum generation source for optical coherence tomography," Opt. Lett. **27**, 2010–2012 (2002).